

Magnifying quantum phase fluctuations with Cooper-pair pairing

W.C. Smith,^{1,2,*} M. Villiers,^{1,2} A. Marquet,^{1,2} J. Palomo,¹ M.R. Delbecq,¹
T. Kontos,¹ P. Campagne-Ibarcq,^{2,1} B. Douçot,³ and Z. Leghtas^{4,1,2,†}

¹Laboratoire de Physique de l'Ecole Normale Supérieure,
ENS, Université PSL, CNRS, Sorbonne Université,

Université Paris-Diderot, Sorbonne Paris Cité, Paris, France

²QUANTIC Team, Inria de Paris, 2 rue Simone Iff, 75012 Paris, France

³Laboratoire de Physique Théorique et Hautes Energies,
Sorbonne Université and CNRS UMR 7589, 4 place Jussieu, 75252 Paris Cedex 05, France

⁴Centre Automatique et Systèmes, Mines-ParisTech,
PSL Research University, 60 bd Saint-Michel, 75006 Paris, France

(Dated: June 30, 2022)

Remarkably, complex assemblies of superconducting wires, electrodes, and Josephson junctions are compactly described by a handful of collective phase degrees of freedom that behave like quantum particles in a potential [1]. The inductive wires contribute a parabolic confinement, while the tunnel junctions add a cosinusoidal corrugation. Usually, the ground state wavefunction is localized within a single potential well—that is, quantum phase fluctuations are small—although entering the regime of delocalization holds promise for metrology and qubit protection [2, 3]. A direct route is to loosen the inductive confinement and let the ground state phase spread over multiple Josephson periods, but this requires a circuit impedance vastly exceeding the resistance quantum and constitutes an ongoing experimental challenge [4]. Here we take a complementary approach and fabricate a generalized Josephson element that can be tuned in situ between one- and two-Cooper-pair tunneling, doubling the frequency of the corrugation and thereby magnifying the number of wells probed by the ground state. We measure a tenfold suppression of flux sensitivity of the first transition energy, implying a twofold increase in the vacuum phase fluctuations.

In superconducting circuits, patterned electrodes are arranged in seemingly endless varieties to build hardware ranging from qubits to amplifiers [5]. Formally, their behavior reduces to that of a particle moving across Josephson potential wells superimposed on a parabolic background due to the circuit inductance. The finite particle mass, provided by the circuit capacitance, induces quantum fluctuations of the position-like degree of freedom—the superconducting phase [6, 7]. These circuits operate predominantly in the regime of small phase fluctuations, where the system ground state resides in a single potential well [8]. What would emerge from circuits whose

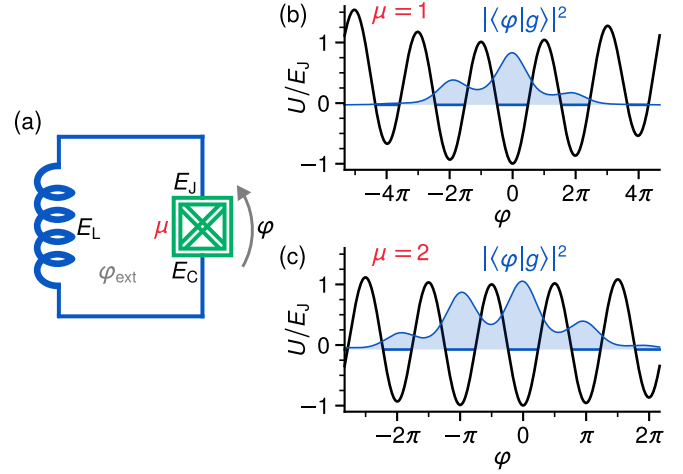


FIG. 1. Principle of magnifying the effective quantum phase fluctuations. (a) Electrical circuit diagram for a generalized Josephson junction (cross-hatched box) shunted by a superinductance. This junction possesses an internal parameter $\mu = 1, 2, \dots$ that specifies the periodicity of the Josephson potential. (b-c) Potential and ground state probability density for the cases $\mu = 1$ and $\mu = 2$, showing the increase in number of Josephson wells accessible to the ground state.

ground states are delocalized among multiple Josephson wells?

Computational states that are spread in phase space over multiple sites are at the root of robust and hardware-efficient encoding of quantum information. In this scheme, the delocalization is engineered to combat, at the Hamiltonian level, the detrimental effects of noise stemming from local sources. The so-called grid states of the Gottesman-Kitaev-Preskill (GKP) error correction code and the $0-\pi$ qubit constitute notable examples [3, 9]. In addition, such circuits could be tiled into topologically protected qubits [10] and employed for fault-tolerant error syndrome measurements [11, 12], the development of quantum phase-slip elements [13], and the observation of Bloch oscillations [2]. Despite the wide scope of application, this regime has remained largely inaccessible.

To understand this, consider a generic superconducting qubit that consists of an inductance, a capacitance, and

* william.smith@ens.fr

† zaki.leghtas@ens.fr

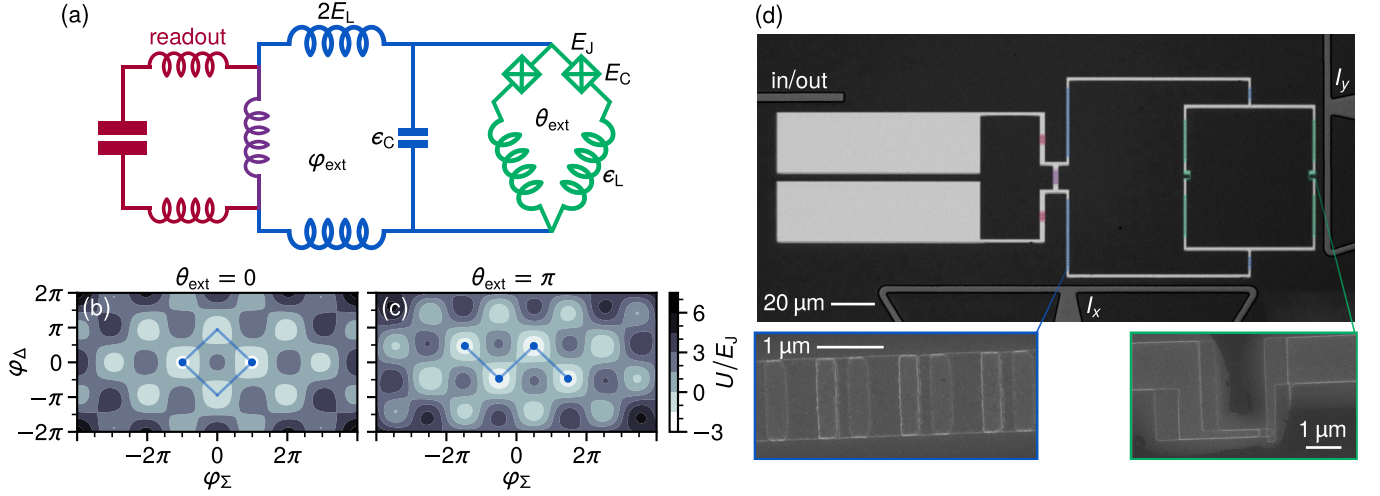


FIG. 2. Schematic of the experimental device. (a) Electrical circuit diagram for the KITE (green) shunted by a superinductance and a capacitance (blue). A lumped LC oscillator (maroon) is added for dispersive readout and couples inductively to the circuit through a shared inductance (purple). (b–c) Potential energy landscape at the external flux bias points $\varphi_{\text{ext}} = \pi$ and $\theta_{\text{ext}} = 0, \pi$. Here, φ_{Σ} and φ_{Δ} are the symmetric and antisymmetric combinations of the phase drops across the two junctions of the KITE. The low-energy physics is dominated by tunneling (semi-transparent blue segments) between the lowest potential wells (solid blue dots). (d) Optical micrograph of the physical device, with aluminum electrodes in light grey and niobium electrodes in dark grey. Direct currents, microwave drives, and readout signals are routed in and out of the system through two on-chip flux bias lines (right and bottom) and one weakly-coupled pin (top left). (Insets) Scanning electron microscope images of one array of large junctions [all inductances pictured in (a) are implemented similarly] and one small junction.

a Josephson junction of energies E_L , E_C , and E_J . Two parameters condition the regime of operation: E_J/E_L , which specifies the number of potential wells, and E_J/E_C , which determines the number of energy levels within a well. Here, the regime of interest corresponds to $E_J/E_C \sim 1$ and $E_J/E_L \gg 1$, implying $E_C/E_L \gg 1$. The latter condition corresponds to a linear circuit with characteristic impedance far exceeding the superconducting resistance quantum, which constitutes a formidable challenge. Initial progress was made using the advent of the superinductance [14], now realized in various materials [15–17]. However, surpassing this threshold by two orders of magnitude has only recently been achieved in a feat of nanofabrication, where Josephson junction arrays were suspended in vacuum [4].

In this Letter, we enter the regime of ground state delocalization by introducing a generalized Josephson element, which can be tuned in situ between two operating points where the potential is 2π - or π -periodic [18, 19]. This doubles the frequency of the corrugation and hence also the number of sites accessible to the ground state. In our experimental realization, we shunt this generalized Josephson element with a conventional superinductance and measure the low-lying transition energies as a function of the external magnetic flux threading the loop. We observe a tenfold suppression of the dispersion of the first excited transition energy in flux, corresponding to a twofold increase in the quantum fluctuations of the phase, which essentially washes out the effects of localization.

The lumped element circuit we aim to implement (rep-

resented in Fig. 1a) is described by the Hamiltonian

$$H_{\mu} = 4E_C \left(\frac{N}{\mu} \right)^2 + \frac{1}{2} E_L (\varphi - \varphi_{\text{ext}})^2 - E_J \cos(\mu\varphi). \quad (1)$$

Here, φ is the gauge-invariant superconducting phase drop across the generalized Josephson element and N is the conjugate number of tunneled Cooper pairs. The external magnetic flux threading the loop is φ_{ext} (in dimensions of phase) and the parameter $\mu = 1, 2, \dots$ specifies the multiplicity of Cooper pairs that tunnel, as can be seen in the charge basis:

$$\cos(\mu\varphi) = \frac{1}{2} \sum_{N=-\infty}^{\infty} (|N\rangle\langle N + \mu| + |N + \mu\rangle\langle N|). \quad (2)$$

In the fluxonium regime $E_L \ll E_C \lesssim E_J$, the ground state is confined to the lowest few potential wells [14]. When the period of the Josephson potential is halved by changing $\mu = 1$ to $\mu = 2$, the ground state delocalization is substantially magnified (see Figs. 1b–1c).

Our implementation of the generalized Josephson element follows the proposal of Ref. [20] (see green portion of Fig. 2a). A superconducting loop is composed of two nearly identical small Josephson junctions, with tunneling energy E_J and charging energy E_C , in parallel and each in series with a superinductance with inductive energy $\epsilon_L \ll E_J$. In contrast with the rhombus [18], we name this dipole element the Kinetic Interference coTunneling Element (KITE). Unlike the rhombus, the KITE does not contain any isolated superconducting

islands and is therefore immune from offset charge noise [19]. The KITE behaves like the generalized Josephson element depicted in Fig. 1a with $\mu = 1$ at the threaded external flux value $\theta_{\text{ext}} = 0$ and $\mu = 2$ at $\theta_{\text{ext}} = \pi$, which we hereafter refer to as zero and half flux. While a single ridge of potential wells at zero flux leads to a spacing of 2π in the symmetric phase φ_{Σ} between adjacent minima (see Fig. 2b), two ridges are interleaved at half flux, reducing the spacing to π (see Fig. 2c and Supplementary Material). We shunt the KITE with a superinductance (blue) of inductive energy E_L , and its associated capacitance of charging energy ϵ_C . The circuit is measured through a lumped LC readout resonator (maroon), which is coupled through a shared inductance (purple). The parameter regime that we operate in is $E_L < \epsilon_L \ll E_J \sim E_C$. All superinductances are implemented with Josephson junction arrays and ϵ_C is determined by the specific geometric arrangement of the connection wires.

We fabricate the circuit by first sputtering niobium over a silicon substrate to define the control lines (see Fig. 2d). Then, a double-angle aluminum evaporation step produces the two small junctions and the 100 total large junctions of the KITE, as well as the 100 large junctions of the shunting superinductance. The number of superinductance junctions was chosen to keep all the self-resonant array modes above 10 GHz [21]. We extract the circuit parameters $E_J/h = 5.9$ GHz, $E_C/h = 6.6$ GHz, $E_L/h = 0.23$ GHz, $\epsilon_L/h = 0.36$ GHz, and $\epsilon_C/h = 2.5$ GHz. The device is then measured in a dilution refrigerator at 10 mK.

We observe the phase response of the readout resonator (see Fig. 3a), which is periodically repelled by transition energies of the circuit (see Figs. 3b–3c), as we sweep the on-chip flux bias currents. Each of the small KITE junctions contributes a cosinusoidal Josephson potential, resulting in a circuit Hamiltonian that is 2π -periodic in both loop fluxes and symmetric about the points $(\varphi_{\text{ext}}, \theta_{\text{ext}}) = (0, 0)$, $(\pi, 0)$, $(0, \pi)$, and (π, π) (see Supplementary Material). These symmetries are observed in the data of Fig. 3a, where we trace the primitive cell closest to the zero-bias point (overlaid lines), which sets the scale and angle of the φ_{ext} and θ_{ext} axes. The mapping between the flux bias currents (I_x, I_y) and $(\varphi_{\text{ext}}, \theta_{\text{ext}})$ is completed by identifying the four points of inversion symmetry within the primitive cell (solid white dots) and labeling them based on the fine energy structure of the system.

We access the transition energies of the circuit in a two-tone spectroscopy experiment at $\theta_{\text{ext}} = 0, \pi$ (see Figs. 4c–4d). For each external flux value φ_{ext} , we calibrate the frequency of a readout tone and measure its reflected phase response as a function of the frequency of a probe tone fed into the I_x port. In order to fully constrain the circuit Hamiltonian identification, we report the fitted center frequencies of all persistent spectral lines visible below 6.6 GHz. We fit the twelve measured transition energies (five at zero flux and seven at half

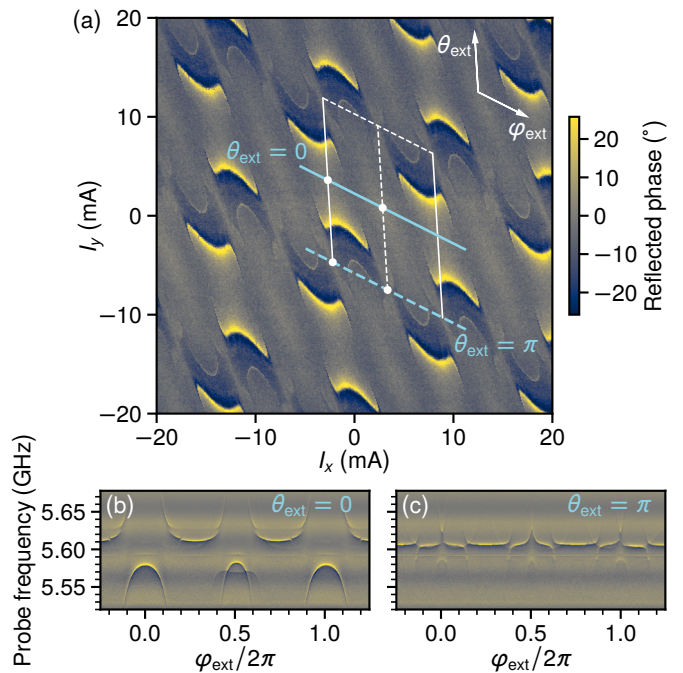


FIG. 3. Device flux dependence. (a) Phase of the reflected probe signal (color) on the readout port, at the fixed probe frequency of 5.595 GHz, as a function of both flux bias currents I_x and I_y . The overlaid lines indicate the independent φ_{ext} and θ_{ext} axes, while dots mark points of inversion symmetry. This phase response signals the periodic approach of the circuit transition energies in the vicinity of the readout resonance. (b–c) Phase of the reflected probe signal (color) on the readout port, as a function of probe frequency and external flux φ_{ext} at zero and half flux [solid and dashed blue lines in (a)], displaying periodic avoided crossings.

flux) to the eigenspectrum of the Hamiltonian of the circuit depicted in Fig. 2a, excluding the readout circuit and parametrized by $\{E_J, E_C, E_L, \epsilon_L\}$ (see Supplementary Material). The remarkable agreement between data and theory is a powerful demonstration that this relatively complex assembly—involving two loops and 215 Josephson junctions—is well captured by a three-mode model with only four independent parameters.

The most essential feature of this spectrum is the drastic reduction of the flux dispersion of the first excited state transition, which spans 1.6 GHz at zero flux and only 140 MHz at half flux (blue circles in Figs. 4c–4d). Since the higher transitions exhibit significant flux dependence, this reduction is a direct signature of the ground and first excited state delocalization over additional Josephson wells. Indeed, as the external flux is increased, the cosinusoidal corrugation slides over the parabolic background. A particle localized in a single Josephson well—known as a fluxon state—would be carried upward in energy until it tunnels to the trailing descending fluxon state, resulting in a large flux dispersion. On the other hand, a delocalized particle simultaneously occupies ascending and descending fluxon states, washing

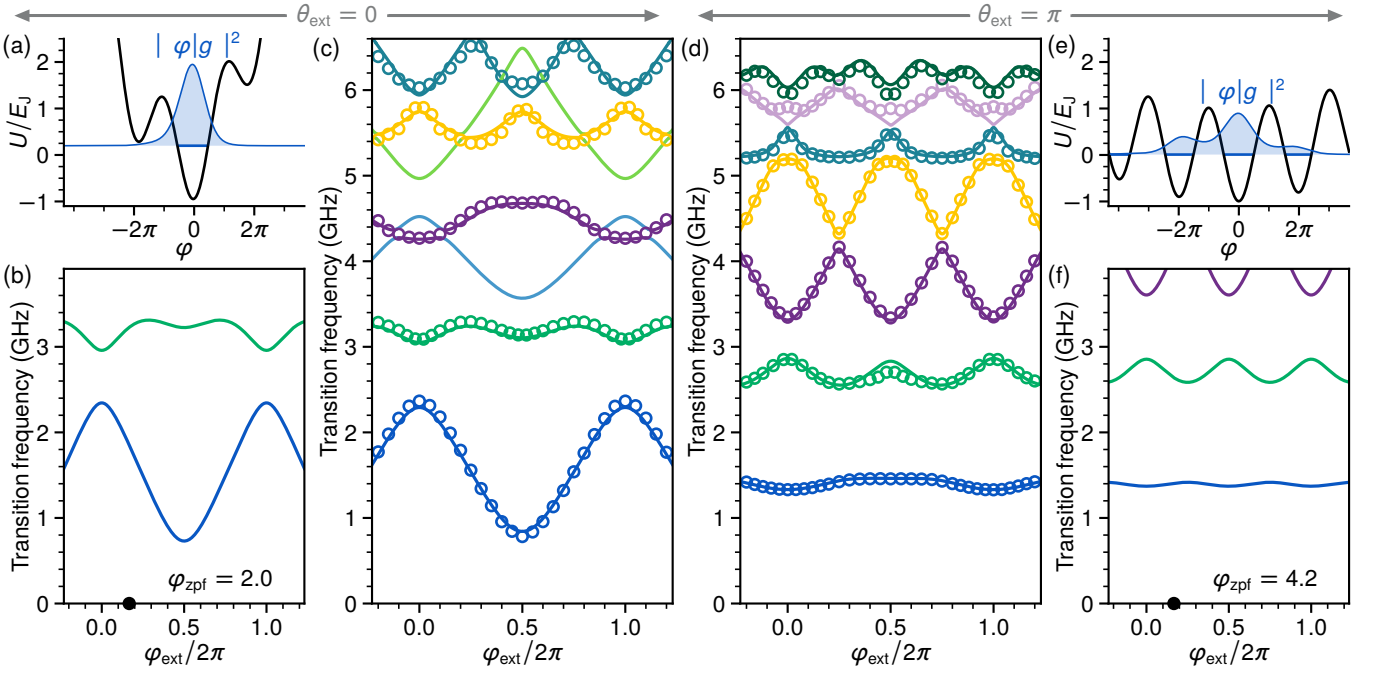


FIG. 4. Magnified effective quantum phase fluctuations. (a,e) Potential energy landscape and ground state probability density at $\varphi_{\text{ext}} = \pi/3$ (black dot in plots beneath) for the cases of zero flux $\theta_{\text{ext}} = 0$ and half flux $\theta_{\text{ext}} = \pi$. (b,f) Lowest-lying transition frequencies of the effective single-mode Hamiltonians at zero and half flux, showing an increase in the amplitude of the zero-point fluctuations of the phase from $\varphi_{\text{zpf}} = 2.0$ to $\varphi_{\text{zpf}} = 4.2$. (c-d) Two-tone measurements of the transition frequencies from the ground state (open circles) and corresponding fitted values (solid curves) obtained from the three-mode circuit. The light blue and light green transitions were not visible in spectroscopy due to their strong decoupling from the readout resonator. The essential feature is the remarkable suppression of flux dispersion of the first excited state transition when θ_{ext} is stepped from 0 to π .

out the flux dependence of the energy.

An additional striking feature of Fig. 4d is the π -periodicity of the energy spectrum at $\theta_{\text{ext}} = \pi$, in stark contrast with the usual 2π -periodicity of a Josephson potential, as observed in Fig. 4c. This effect is slightly diminished by residual asymmetry in the areas of the two small KITE junctions, which we find to be around 6%. Finally, note the two transitions at zero flux (light blue and light green lines in Fig. 4c) predicted by theory but not observed in the experiment. This is explained by the vanishingly small dispersive coupling of these transitions to the readout resonator, as predicted by circuit quantization (see Supplementary Material).

Although a three-mode model was necessary to capture the complete energy spectrum up to 6.6 GHz, the first few transition energies are well described by the emergent low-energy Hamiltonian of Eq. 1, with only a single collective degree of freedom. Indeed, merely inserting the previously fitted values of E_J , E_C , an inductive energy $[E_L^{-1} + (2\epsilon_L)^{-1}]^{-1}$ into Eq. 1 with $\mu = 2$ (see Supplementary Material), we recover the first two transitions at half flux, as shown in Fig. 4f. In the rescaled coordinates $\varphi \rightarrow \varphi/\mu$ and $N \rightarrow \mu N$, the amplitude of the zero-point fluctuations of the phase across the general-

ized Josephson element is given by

$$\varphi_{\text{zpf}} = \left(\frac{2E_C}{E_L} \mu^2 \right)^{1/4}. \quad (3)$$

Incrementing μ from one to two magnifies φ_{zpf} by a factor $\sqrt{2}$. Putting this into perspective, this is the enhancement that would be obtained from reducing the capacitance to ground in a Josephson junction array by a factor of sixteen, allowing a fourfold increase in the total linear inductance, a strategy followed by Ref. [4]. Note that in the experiment we observe a larger magnification factor because the effective behavior of our circuit at $\theta_{\text{ext}} = 0$ involves double-phase-slip processes (see Supplementary Material). We find $\varphi_{\text{zpf}} = 4.2 \pm 0.2$, which is strictly larger than π , therefore unambiguously placing our system in the regime of ground state delocalization.

An ongoing quest in quantum information science is to build a circuit that hosts a degenerate ground state manifold that encodes and protects quantum states. A particularly appealing approach is to combine a generalized Josephson element with the so-called quantum phase-slip element [13], the dual of the Josephson junction [22]. Such a circuit would encode information in the form of GKP states [9] that are protected at the Hamiltonian level, circumventing the need for error syndrome measurements and feedback. The key technological innova-

tion of our experiment—the KITE—is an implementation of such a generalized Josephson element.

In conclusion, we have entered the regime of ground state delocalization using a superconducting circuit comprised only of conventional Josephson junction arrays. This was made possible by our particular arrangement of these dipoles, from which emerges a generalized Josephson element that exclusively permits the tunneling of pairs of Cooper pairs, thereby increasing the number of Josephson wells that host the ground state wavefunction. This remarkable spread corresponds to effectively magnified quantum fluctuations of the superconducting phase, inferred from the measured suppression of the flux dispersion of the first excited state transition to be $\varphi_{\text{zpf}} = 4.2 \pm 0.2$. We envision incorporating a quantum phase-slip element into our circuit to implement a protected qubit, observe the quantum dynamics of nonlocal operators, and perform fault-tolerant error syndrome measurements [11, 12].

Acknowledgments: We thank Raphaël Lescanne and Mazyar Mirrahimi for fruitful discussions, and Lincoln Labs for providing a Josephson Traveling-Wave Parametric Amplifier. Z.L. acknowledges support from ANR project ENDURANCE, and EMERGENCE grant ENDURANCE of Ville de Paris. The devices were fabricated within the consortium Salle Blanche Paris Centre. This work has been supported by the Paris Île-de-France Region in the framework of DIM SIRTEQ. This project has received funding from the European Research Council (ERC) under the European Union’s Horizon 2020 research and innovation programme (grant agreement No. 851740).

Author contributions: W.C.S. conceived the experiment and measured the device. W.C.S., assisted by A.M., designed the sample, which Z.L. fabricated. W.C.S., Z.L., B.D., and P.C.-I. analyzed the data. M.V., J.P., T.K., and M.R.D. provided experimental support. W.C.S. and Z.L. co-wrote the manuscript with input from all authors.

-
- [1] J. Clarke, A. N. Cleland, M. H. Devoret, D. Esteve, and J. M. Martinis, Quantum mechanics of a macroscopic variable: The phase difference of a Josephson junction, *Science* **239**, 992 (1988).
 - [2] F. Piquemal and G. Genevès, Argument for a direct realization of the quantum metrological triangle, *Metrologia* **37**, 207 (2000).
 - [3] A. Kitaev, Protected qubit based on a superconducting current mirror, [arXiv:cond-mat/0609441](https://arxiv.org/abs/cond-mat/0609441) (2006).
 - [4] I. V. Pechenezhskiy, R. A. Mencia, L. B. Nguyen, Y.-H. Lin, and V. E. Manucharyan, The superconducting quasicharge qubit, *Nature* **585**, 368 (2020).
 - [5] M. H. Devoret and R. J. Schoelkopf, Superconducting circuits for quantum information: An outlook, *Science* **339**, 1169 (2013).
 - [6] M. H. Devoret, Quantum fluctuations in electrical circuits, in *Quantum Fluctuations (Les Houches Session LXIII)*, edited by S. Reynaud, E. Giacobino, and J. Zinn-Justin (North-Holland, 1997) pp. 351–386.
 - [7] S. M. Girvin, Circuit QED: Superconducting qubits coupled to microwave photons, in *Quantum Machines: Measurement and Control of Engineered Quantum Systems (Les Houches Session XCVI)*, edited by M. Devoret, B. Huard, R. Schoelkopf, and L. F. Cugliandolo (Oxford University Press, 2014) pp. 113–256.
 - [8] M. Kjaergaard, M. E. Schwartz, J. Braumüller, P. Krantz, J. I.-J. Wang, S. Gustavsson, and W. D. Oliver, Superconducting qubits: Current state of play, *Annu. Rev. Condens. Matter Phys.* **11**, 369 (2020).
 - [9] D. Gottesman, A. Kitaev, and J. Preskill, Encoding a qubit in an oscillator, *Phys. Rev. A* **64**, 012310 (2001).
 - [10] B. Douçot and L. B. Ioffe, Physical implementation of protected qubits, *Rep. Prog. Phys.* **75**, 072001 (2012).
 - [11] P. Brooks, A. Kitaev, and J. Preskill, Protected gates for superconducting qubits, *Phys. Rev. A* **87**, 052306 (2013).
 - [12] J. Cohen, W. C. Smith, M. H. Devoret, and M. Mirrahimi, Degeneracy-preserving quantum nondemolition measurement of parity-type observables for cat qubits, *Phys. Rev. Lett.* **119**, 060503 (2017).
 - [13] J. E. Mooij and Y. V. Nazarov, Superconducting nanowires as quantum phase-slip junctions, *Nature Physics* **2**, 169 (2006).
 - [14] V. E. Manucharyan, J. Koch, L. I. Glazman, and M. H. Devoret, Fluxonium: Single Cooper-pair circuit free of charge offsets, *Science* **326**, 113 (2009).
 - [15] L. Grünhaupt, M. Spiecker, D. Gusenkova, N. Maleeva, S. T. Skacel, I. Takmakov, F. Valenti, P. Winkel, H. Rotzinger, W. Wernsdorfer, A. V. Ustinov, and I. M. Pop, Granular aluminium as a superconducting material for high-impedance quantum circuits, *Nature Materials* **18**, 816 (2019).
 - [16] M. Pita-Vidal, A. Bargerbos, C.-K. Yang, D. J. van Woerkom, W. Pfaff, N. Haider, P. Krogstrup, L. P. Kouwenhoven, G. de Lange, and A. Kou, A gate-tunable, field-compatible fluxonium, [arXiv:1910.07978](https://arxiv.org/abs/1910.07978) (2019).
 - [17] M. Peruzzo, A. Trioni, F. Hassani, M. Zemlicka, and J. M. Fink, Surpassing the resistance quantum with a geometric superinductor, [arXiv:2007.01644](https://arxiv.org/abs/2007.01644) (2020).
 - [18] G. Blatter, V. B. Geshkenbein, and L. B. Ioffe, Design aspects of superconducting-phase quantum bits, *Phys. Rev. B* **63**, 174511 (2001).
 - [19] S. Gladchenko, D. Olaya, E. Dupont-Ferrier, B. Doucot, L. B. Ioffe, and M. E. Gershenson, Superconducting nanocircuits for topologically protected qubits, *Nat. Phys.* **5**, 48 (2009).
 - [20] W. C. Smith, A. Kou, X. Xiao, U. Vool, and M. H. Devoret, Superconducting circuit protected by two-Cooper-pair tunneling, *npj Quantum Inf.* **6**, 8 (2020).
 - [21] N. A. Masluk, I. M. Pop, A. Kamal, Z. K. Mineev, and M. H. Devoret, Microwave characterization of Josephson junction arrays: Implementing a low loss superinductance, *Phys. Rev. Lett.* **109**, 137002 (2012).
 - [22] D. T. Le, A. Grimsmo, C. Müller, and T. M. Stace, Doubly nonlinear superconducting qubit, *Phys. Rev. A* **100**, 062321 (2019).

Supplementary material: Magnifying quantum phase fluctuations with Cooper-pair pairing

W. C. Smith,* M. Villiers, A. Marquet, J. Palomo, M. R. Delbecq,
T. Kontos, P. Campagne-Ibarcq, B. Douçot, and Z. Leghtas†
(Dated: June 30, 2022)

S1. DEVICE FABRICATION

The circuit is fabricated on a 280 μm -thick wafer of intrinsic silicon (resistivity exceeding 10 000 $\Omega\text{ cm}$). The silicon wafer is cleaned in solvents and loaded in a sputtering system. After one night of pumping, we start with an argon milling cleaning step, and proceed to sputter 120 nm of niobium onto the chip. We spin optical resist (S1805), and pattern the large features (control lines) with a laser writer. After development (MF319), we etch the sample in SF6 with a 20 s overetch, followed by lift off (acetone at 50 $^{\circ}\text{C}$). We then spin a bilayer of MAA (EL11) and PMMA (A6). The entire circuit (KITE, inductive shunt, and readout resonator) is patterned in an e-beam lithography step. The development takes place in a 3:1 IPA/water solution at 6 $^{\circ}\text{C}$ for 90 s, followed by 10 s in IPA. The chip is then loaded in an e-beam evaporator. We start with a thorough argon ion milling for 2 min with the sample forming an angle of $\pm 30^{\circ}$ which serves the purpose of cleaning the substrate. We then evaporate 35 nm and 70 nm of aluminum, at $\pm 30^{\circ}$ angles, separated by an oxidation step of 200 mbar of pure oxygen for 10 min.

The Josephson junctions are all fabricated from Al/AlOx/Al in a single evaporation step, using the Dolan bridge method with an e-beam base dose of 283 $\mu\text{C cm}^{-2}$, and come in three types. (i) Two small junctions in the KITE of area 0.075 μm^2 , made in a cross geometry, patterned with a dose factor of 1.6, and resulting in an inductance per junction of 52 nH. (ii) A total of 100 large array junctions within the KITE loop and a total of 100 unshared shunting array junctions, of area 0.49 μm^2 , patterned with a dose factor of 1.8, and resulting in an inductance per junction of 6.8 nH. (iii) Thirteen larger array junctions that form the readout resonator inductance (seven of which are shared) of area 1.10 μm^2 , patterned with a dose factor of 1.5, and resulting in an inductance per junction of 3.45 nH.

The chip was subsequently baked at 115 $^{\circ}\text{C}$ for 1 min, glued with PMMA onto a PCB, wire-bonded and mounted into a sample holder. The device was then thermally anchored to the base plate of a Bluefors dilution refrigerator, surrounded by three concentric cans for magnetic and infrared shielding (outer: cryoperm, middle: aluminum, inner: copper). An optical micrograph of the circuit and SEM images of some junctions are shown in Fig. 2d.

S2. CIRCUIT QUANTIZATION

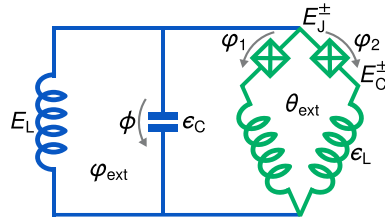


FIG. S1. Equivalent electrical circuit diagram to Fig. 2a, with series arrangements of linear inductances combined and the readout mode neglected. Additionally, the two small Josephson junctions are allowed to have slightly differing areas, so $E_J^{\pm} = (1 \pm \epsilon)E_J$ and $E_C^{\pm} = E_C/(1 \pm \epsilon)$, with ϵ being a small asymmetry parameter.

To quantize the circuit in Fig. 2a, we first combine all series occurrences of linear inductances, as justified by Kirchhoff's current law. This yields the mathematically equivalent circuit in Fig. S1. This circuit has three degrees

* william.smith@ens.fr

† zaki.leghtas@ens.fr

of freedom: two corresponding to the KITE and one to the shunting circuit. Note that we have discarded the readout mode, as it does not significantly affect the energy levels of the remaining circuit. Additionally, the energy scales correspond to the respective capacitances and inductances of the circuit according to

$$E_C = \frac{e^2}{2C_J} \quad \epsilon_C = \frac{e^2}{2C} \quad E_J = \frac{\phi_0^2}{L_J} \quad E_L = \frac{\phi_0^2}{L} \quad \epsilon_L = \frac{\phi_0^2}{\ell}, \quad (\text{S1})$$

where $\phi_0 = \hbar/2e$ is the reduced magnetic flux quantum. We obtain the Hamiltonian [1]

$$H = \frac{2E_C}{1-\epsilon^2}(N_\Sigma^2 + N_\Delta^2 - 2\epsilon N_\Sigma N_\Delta) + 4\epsilon_C n^2 + \frac{1}{2}E_L \phi^2 + \epsilon_L (\phi - \varphi_\Sigma - \varphi_{\text{ext}} - \frac{1}{2}\theta_{\text{ext}})^2 + \epsilon_L (\varphi_\Delta - \frac{1}{2}\theta_{\text{ext}})^2 - 2E_J \cos \varphi_\Sigma \cos \varphi_\Delta + 2\epsilon E_J \sin \varphi_\Sigma \sin \varphi_\Delta. \quad (\text{S2})$$

Due to the high degree of symmetry in the KITE, we have introduced the symmetric and antisymmetric variables $\varphi_\Sigma = \frac{1}{2}(\varphi_1 + \varphi_2)$ and $\varphi_\Delta = \frac{1}{2}(\varphi_1 - \varphi_2)$ in the above. Note also that $\{N_\Sigma, N_\Delta, n\}$ are the conjugate Cooper pair numbers to $\{\varphi_\Sigma, \varphi_\Delta, \phi\}$. Numerical diagonalization of Eq. S2 is readily carried out in the three-mode Fock basis [2].

Although we have neglected the readout mode in Eq. S2, we note that it directly couples to the ϕ mode exclusively. Since the ϕ variable hybridizes significantly with φ_Σ , but not φ_Δ , we expect only a subset of the eigenstates to dispersively shift the readout resonance at external flux values where φ_Σ and φ_Δ are roughly independent. This is the case at $\theta_{\text{ext}} = 0$ but not $\theta_{\text{ext}} = \pi$, explaining the invisibility of certain higher frequency transitions in Fig. 4c.

S3. MODEL REDUCTION

In this section, we describe the mathematical procedure for reducing the three-mode Hamiltonian in Eq. S2 to an effective one-mode Hamiltonian at the KITE bias values $\theta_{\text{ext}} = \pi, 0$. The main purpose of these approximations is to extract an effective amplitude of quantum phase fluctuations, and thereby benchmark the extent of observed ground state delocalization.

A. Born-Oppenheimer approximation

We place ourselves in the regime where $E_L < \epsilon_L \ll E_J \sim E_C$ and $\epsilon \ll 1$ in Eq. S2. Furthermore, we are chiefly interested in the limit where ϵ_C is the dominant energy scale, i.e. the limit of small shunt capacitance. While we did not strictly achieve this experimentally due to our specific circuit geometry, this limit conveniently reveals the relevant underlying physics of the circuit. In Born-Oppenheimer theory, one considers a system with a collection of high-frequency electron-like degrees of freedom and a collection of low-frequency nucleus-like degrees of freedom. To obtain an approximate Hamiltonian for the “nuclei,” one freezes the “electrons” in their quantum ground state, which is found by fixing the nuclear variables to their classical values. In our system, we regard the ϕ variable as high-frequency and treat the φ_Σ and φ_Δ variables as low-frequency. Fixing φ_Σ and φ_Δ to their classical values and setting N_Σ and N_Δ to zero, Eq. S2 reduces to

$$H_e = 4\epsilon_C n^2 + \frac{1}{2}E_L \phi^2 + \epsilon_L (\phi - \varphi_\Sigma - \varphi_{\text{ext}} - \frac{1}{2}\theta_{\text{ext}})^2. \quad (\text{S3})$$

Note that, in this equation, ϕ and n are operators while φ_Σ is a parameter. This Hamiltonian simply describes a harmonic oscillator whose equilibrium position is set by φ_Σ (in addition to the other Hamiltonian parameters). We can hence readily identify the energy levels of H_e as

$$E_{e,m} = \sqrt{8(E_L + 2\epsilon_L)\epsilon_C} \left(m + \frac{1}{2}\right) + \frac{E_L \epsilon_L}{E_L + 2\epsilon_L} (\varphi_\Sigma + \varphi_{\text{ext}} + \frac{1}{2}\theta_{\text{ext}})^2. \quad (\text{S4})$$

We may then plug this into Eq. S2 to obtain the effective low-energy Hamiltonian

$$H_n = \frac{2E_C}{1-\epsilon^2}(N_\Sigma^2 + N_\Delta^2 - 2\epsilon N_\Sigma N_\Delta) + \frac{E_L \epsilon_L}{E_L + 2\epsilon_L} (\varphi_\Sigma + \varphi_{\text{ext}} + \frac{1}{2}\theta_{\text{ext}})^2 + \epsilon_L (\varphi_\Delta - \frac{1}{2}\theta_{\text{ext}})^2 - 2E_J \cos \varphi_\Sigma \cos \varphi_\Delta + 2\epsilon E_J \sin \varphi_\Sigma \sin \varphi_\Delta + \sqrt{8(E_L + 2\epsilon_L)\epsilon_C} \left(m + \frac{1}{2}\right). \quad (\text{S5})$$

Recall that here, φ_Σ and φ_Δ have been restored as operators (as well as N_Σ and N_Δ), while ϕ has been reduced to the discrete parameter $m = 0, 1, \dots$ (playing the role of an orbital index) while also modifying the energy landscape of φ_Σ . Note that the solutions to H_n can only be expected to resemble those to the full Hamiltonian for energies smaller than $\sqrt{8(E_L + 2\epsilon_L)\epsilon_C}$. For our experimental parameters, this cutoff corresponds to a frequency of 4.35 GHz, which makes this analysis relevant for the first two transitions only. Furthermore, the inductive energy for φ_Σ corresponds to that for a series arrangement of inductances L and $\ell/2$ (a parallel arrangement of two inductances ℓ).

B. Projection at $\theta_{\text{ext}} = \pi$

Restricting our attention to the case of symmetric junctions, we consider Eq. S5 for $m = 0$,

$$H_\pi = 2E_C(N_\Sigma^2 + N_\Delta^2) + \frac{E_L\epsilon_L}{E_L + 2\epsilon_L}(\varphi_\Sigma + \varphi_{\text{ext}})^2 + \epsilon_L\varphi_\Delta^2 + 2E_J \sin \varphi_\Sigma \sin \varphi_\Delta. \quad (\text{S6})$$

Since E_J is the dominant energy scale, we first consider the locations at which the Josephson tunneling energy is minimized: $\varphi_\Sigma = (m_\Sigma + \frac{1}{2})\pi$ and $\varphi_\Delta = (m_\Delta + \frac{1}{2})\pi$ where m_Σ and m_Δ are integers with the same parity. Due to their small energy scales, the linearly inductive terms only contribute a broad parabolic confinement centered at $\varphi_\Sigma = -\varphi_{\text{ext}}$ and $\varphi_\Delta = 0$. It is then natural to introduce a two-dimensional tight-binding model with individual sites corresponding to the different Josephson wells. To this end, we arrive at the Hamiltonian

$$H_\pi^{\text{tight-binding,2D}} = \sum_{\{m_\Sigma + m_\Delta \text{ even}\}} \left[\frac{E_L\epsilon_L}{E_L + 2\epsilon_L} (m_\Sigma\pi + \frac{\pi}{2} + \varphi_{\text{ext}})^2 + \epsilon_L (m_\Delta\pi + \frac{\pi}{2})^2 \right] |m_\Sigma, m_\Delta\rangle \langle m_\Sigma, m_\Delta| \\ + \sum_{\{m_\Sigma + m_\Delta \text{ even}\}} \frac{1}{2} \Gamma (|m_\Sigma, m_\Delta\rangle \langle m_\Sigma \pm 1, m_\Delta \pm 1| + |m_\Sigma \pm 1, m_\Delta \pm 1\rangle \langle m_\Sigma, m_\Delta|), \quad (\text{S7})$$

where the index $\{m_\Sigma + m_\Delta \text{ even}\}$ indicates summation over only the lowest potential minima and the hopping energy Γ corresponds to the nearest-neighbor tunneling rate for the lowest wells. The factor of $1/2$ accounts for double counting and the hopping rate coincides with the standard result for the phase-slip rate across a single Josephson junction of tunneling energy E_J and charging energy E_C [3],

$$\Gamma = \frac{4}{\sqrt{\pi}} (8E_J^3 E_C)^{1/4} \exp \left(-\sqrt{\frac{8E_J}{E_C}} \right). \quad (\text{S8})$$

Indeed, this is the phase-slip rate across a single KITE junction because $E_L < \epsilon_L \ll E_J$. Note that we have neglected the effect of double phase slips, that is, transitions $m_{\Sigma,\Delta} \rightarrow m_{\Sigma,\Delta} \pm 2$ with $m_{\Delta,\Sigma}$ unchanged.

Inspection of Eq. S7 shows that, at all values of the external flux φ_{ext} , there are essentially two degenerate lowest rungs of potential wells at $m_\Delta = -1, 0$. This feature makes it possible to draw a zig-zag path through the $\varphi_\Sigma\varphi_\Delta$ -plane that connects all the relevant low-lying potential minima (see Fig. 2c). To this end, we introduce a new tight-binding site index s and write the one-dimensional Hamiltonian

$$H_\pi^{\text{tight-binding,1D}} = \sum_{\{s\}} \frac{E_L\epsilon_L}{E_L + 2\epsilon_L} (s\pi + \frac{\pi}{2} + \varphi_{\text{ext}})^2 |s\rangle \langle s| + \sum_{\{s\}} \frac{1}{2} \Gamma (|s\rangle \langle s+1| + |s+1\rangle \langle s|), \quad (\text{S9})$$

where the index $\{s\}$ again indicates summation over only the lowest potential minima. In the above, the most important feature is that neighboring sites are separated by a distance of π , rather than the conventional 2π . It is interesting to note that s in Eq. S9 plays the role of a fluxon index, in the sense that transitions between neighboring sites involve a single fluxon tunneling in or out of the KITE. Moreover, this Hamiltonian is formally identical to that of the usual Cooper pair box under the interchange of Cooper pair number with fluxon occupation. We therefore conclude that the regime of ground state delocalization—where the tight-binding approximation holds—is also the regime where the circuit begins to behave like a quantum phase-slip element [4].

We then observe that Eq. S9 is also obtained from the continuous Hamiltonian

$$\tilde{H}_\pi = E_C N^2 + \frac{E_L\epsilon_L}{E_L + 2\epsilon_L} (\varphi + \varphi_{\text{ext}})^2 + E_J \cos 2\varphi. \quad (\text{S10})$$

This model must be treated with caution; its spectrum is only expected to resemble that of Eq. S9 for the lowest-energy eigenstates and there are high-energy eigenstates of Eq. S10 that have no counterpart in Eq. S9. As such, we present the eigenspectrum obtained by numerical diagonalization of \tilde{H}_π in Fig. 4f with no fitted parameters. Finally, in order to benchmark the ground state delocalization, we now define the effective amplitude of zero-point fluctuations of the superconducting phase [5],

$$\varphi_{\text{zpf},\pi} = \left(8E_C \frac{E_L + 2\epsilon_L}{2E_L\epsilon_L} \right)^{1/4}. \quad (\text{S11})$$

C. Projection at $\theta_{\text{ext}} = 0$

Following the same procedure as in the previous section, we start with the Hamiltonian

$$H_0 = 2E_C(N_\Sigma^2 + N_\Delta^2) + \frac{E_L\epsilon_L}{E_L + 2\epsilon_L}(\varphi_\Sigma + \varphi_{\text{ext}})^2 + \epsilon_L\varphi_\Delta^2 - 2E_J \cos \varphi_\Sigma \cos \varphi_\Delta \quad (\text{S12})$$

and observe that the relevant minima are located at $\varphi_\Sigma = m_\Sigma\pi$ and $\varphi_\Delta = m_\Delta\pi$ where m_Σ and m_Δ are again integers with the same parity. Here, we arrive the tight-binding Hamiltonian

$$H_0^{\text{tight-binding, 2D}} = \sum_{\{m_\Sigma + m_\Delta \text{ even}\}} \left[\frac{E_L\epsilon_L}{E_L + 2\epsilon_L}(m_\Sigma\pi + \varphi_{\text{ext}})^2 + \epsilon_L(m_\Delta\pi)^2 \right] |m_\Sigma, m_\Delta\rangle \langle m_\Sigma, m_\Delta| \\ + \sum_{\{m_\Sigma + m_\Delta \text{ even}\}} \frac{1}{2} \Gamma (|m_\Sigma, m_\Delta\rangle \langle m_\Sigma \pm 1, m_\Delta \pm 1| + |m_\Sigma \pm 1, m_\Delta \pm 1\rangle \langle m_\Sigma, m_\Delta|) , \quad (\text{S13})$$

which crucially differs from Eq. S7 in the $\pi/2$ offsetted equilibrium positions in the first line.

Examination of Eq. S13 reveals that, at all values of the external flux φ_{ext} , there is a lowest rung of potential wells at $m_\Delta = 0$ and two degenerate next-lowest rungs at $m_\Delta = \pm 1$. Consequently, it is nontrivial to draw a one-dimensional path through the $\varphi_\Sigma\varphi_\Delta$ -plane onto which to adequately project the dynamics, as we did at $\theta_{\text{ext}} = \pi$. Nonetheless, in order to model the lowest energy transitions, we introduce the phenomenological one-dimensional Hamiltonian

$$\tilde{H}_0 = 4\tilde{E}_C N^2 + \frac{E_L\epsilon_L}{E_L + 2\epsilon_L}(\varphi + \varphi_{\text{ext}})^2 - \tilde{E}_J \cos \varphi . \quad (\text{S14})$$

Note here that \tilde{E}_J and \tilde{E}_C are effective Josephson and charging energies. The energy spectrum obtained by numerical diagonalization of \tilde{H}_0 , with parameters $\tilde{E}_J/h = 1.66$ GHz and $\tilde{E}_C/h = 1.48$ GHz determined by a fit to the data, is shown in Fig. 4b. Here, φ is a collective degree of freedom that experiences the same parabolic confinement as the φ_Σ variable in Eq. S12. As above, we define the effective amplitude of zero-point fluctuations of the phase

$$\varphi_{\text{zpf},0} = \left(2\tilde{E}_C \frac{E_L + 2\epsilon_L}{2E_L\epsilon_L} \right)^{1/4} . \quad (\text{S15})$$

S4. SPECTRUM FITTING

We fit the twelve measured transition frequencies shown in Figs. 4c–4d to the eigenspectrum of Eq. S2. In total this Hamiltonian has six parameters: E_J , E_C , E_L , ϵ_L , ϵ_C , and ϵ . We initialize our guess of E_J , E_L , and ϵ_L using normal resistance measurements and the Ambegaokar-Baratoff formula, and start by setting ϵ to zero. Then, assuming a plasma frequency of 17.6 GHz, consistent with previous measurements in our laboratory at similar oxidation parameters, we infer E_C . In order to determine ϵ_C , which is mainly due to the capacitance of the metallic lines in the circuit, we run a finite-element simulation (Ansys HFSS) of the circuit, with all array junctions replaced by linear inductances and the two small junctions of the KITE replaced by capacitances. The simulation provides the frequency of a mode resembling the φ_Σ mode. We then numerically find ϵ_C —in a lumped element circuit corresponding to the HFSS model—that matches the simulated frequency, ultimately finding $\epsilon_C = 2.5$ GHz, which corresponds to a shunt capacitance of $C = 7.7$ fF.

We use all these values to initialize a least-squares fit of the measured transition frequencies to fine tune the four independent parameters E_J , E_C , E_L , and ϵ_L . Note that, as per the discussion at the end of Sec. S2, we do not expect every energy transition to be easily visible in our spectroscopic measurement setup through the readout mode, and therefore appropriate fitting requires a filtering of different energy levels. Indeed, the readout mode couples to the circuit through φ_Σ , and therefore in the fit routine, we neglect the transition to a given state $|i\rangle$ when $|\langle i|\varphi_\Sigma|g\rangle| \ll |\langle i|\varphi_\Delta|g\rangle|$. Finally, we improve the fit by ramping up the asymmetry parameter to $\epsilon = 0.03$, which corresponds to 6% relative asymmetry.

S5. EXTERNAL FLUX CALIBRATION

We have observed that the external magnetic flux drifts on the order of $0.02\Phi_0$, where $\Phi_0 = h/2e$ is the magnetic flux quantum, on a timescale of 24 h. Therefore, we calibrate the external magnetic flux axes φ_{ext} and θ_{ext} daily. To this end, we monitor the readout resonator response as a function of I_x and I_y over a narrow range around three symmetry points, as shown in Fig. S2.

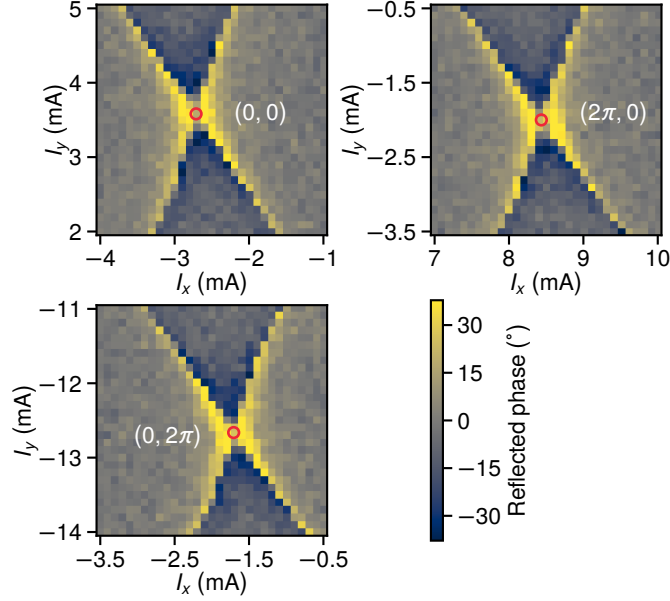


FIG. S2. Typical external flux calibration data. Phase of the reflected probe signal (color) on the readout port, at the fixed probe frequency of 5.580 GHz, as a function of both flux bias currents I_x and I_y . The three panels correspond to zoomed-in portions of Fig. 3a, about the inversion-symmetric points $(\varphi_{\text{ext}}, \theta_{\text{ext}}) = (0, 0)$, $(2\pi, 0)$, and $(0, 2\pi)$. Red circles indicate symmetry points extracted using image inversion convolution, and are used to fully determine the mapping from (I_x, I_y) onto $(\varphi_{\text{ext}}, \theta_{\text{ext}})$.

S6. COHERENCE TIMES

$(\varphi_{\text{ext}}, \theta_{\text{ext}})$	$\omega_{ge}/2\pi$ (GHz)	χ (MHz)	T_1 (μs)	T_{2R} (μs)	T_{2E} (μs)
$(0, 0)$	2.366	31	4.9	0.50	2.0
$(\pi, 0)$	0.792	-12	40	0.48	2.4
$(0, \pi)$	1.329	-30	16	0.43	4.0
(π, π)	1.460	-33	9.2	0.33	1.9

TABLE S1. Coherence properties at the four distinct two-dimensional external flux sweet spots for the first excited state transition. Here, χ denotes the dispersive shift on the readout resonator, T_1 denotes the relaxation time, T_{2R} denotes the Ramsey decoherence time, and T_{2E} denotes the spin-echo decoherence time.

In addition to the spectroscopy data shown in Figs. 4c–4d, we also measured the coherence times and dispersive shifts on the readout resonator by first calibrating a π -pulse from measured Rabi oscillations. The relatively large values of dispersive shift originate from the mutual inductance between the readout and circuit (shared junctions), which was designed to comprise a significant fraction of the readout resonator inductance. The relaxation times essentially follow a trend based on the transition frequency, suggesting that they are limited by dielectric loss. The small coherence times are likely due to flux noise exaggerated by the large loop sizes used in the circuit (see Fig. 2d). This is consistent with the significant improvement in coherence time when adding a single echo pulse. Additionally, we suspect phase slips in the array junctions to contribute to dephasing.

-
- [1] M. H. Devoret, Quantum fluctuations in electrical circuits, in *Quantum Fluctuations (Les Houches Session LXIII)*, edited by S. Reynaud, E. Giacobino, and J. Zinn-Justin (North-Holland, 1997) pp. 351–386.
 - [2] W. C. Smith, A. Kou, U. Vool, I. M. Pop, L. Frunzio, R. J. Schoelkopf, and M. H. Devoret, Quantization of inductively shunted superconducting circuits, *Phys. Rev. B* **94**, 144507 (2016).
 - [3] K. A. Matveev, A. I. Larkin, and L. I. Glazman, Persistent current in superconducting nanorings, *Phys. Rev. Lett.* **89**, 096802 (2002).
 - [4] J. E. Mooij and Y. V. Nazarov, Superconducting nanowires as quantum phase-slip junctions, *Nature Physics* **2**, 169 (2006).

- [5] S. M. Girvin, Circuit QED: Superconducting qubits coupled to microwave photons, in *Quantum Machines: Measurement and Control of Engineered Quantum Systems (Les Houches Session XCVI)*, edited by M. Devoret, B. Huard, R. Schoelkopf, and L. F. Cugliandolo (Oxford University Press, 2014) pp. 113–256.